Mutual Coupling Between Reduced Surface-Wave Microstrip Antennas

Michael A. Khayat, *Student Member, IEEE,* Jeffery T. Williams, *Senior Member, IEEE,* David R. Jackson, *Fellow, IEEE,* and Stuart A. Long, *Fellow, IEEE*

***Abstract*—An investigation of the mutual coupling between reduced surface-wave microstrip antennas is presented and compared with that for conventional microstrip antennas. Numerical results are presented from a theoretical analysis of the mutual coupling along with confirming experimental results. It is shown that for electrically thin substrates, the space-wave coupling, not the surface-wave coupling, is predominant for typical element spacing, for both the conventional and reduced surface-wave antennas. In addition, the mutual coupling behavior is examined using an asymptotic analysis, which demonstrates how the coupling falls off much faster with patch separation for reduced surface wave antennas compared to conventional microstrip patch antennas.**

***Index Terms*—Antenna array mutual coupling, microstrip antennas, printed antennas, surface waves.**

I. Introduction

REDUCED surface-wave (RSW) microstrip antennas are a new class of microstrip radiators that produce only a small amount of surface-wave excitation [1], [2]. If these antennas are printed on an electrically thin substrate, they also only weakly excite a lateral wave field [3]–[5]. (The lateral-wave field is the continuous spectrum or "radiation field"—the total field minus the surface-wave field—that propagates along the air-dielectric interface far away from the antenna.) As a result, these antennas do not suffer from the deleterious effects of surface- and lateral-wave scattering, or the mutual coupling associated with the surface and lateral waves. These characteristics make the RSW antenna ideal for applications where the supporting substrate or ground plane of the antenna is small, in which case diffraction of surface and lateral waves from the edges of the structure may be quite significant for conventional microstrip antennas [6]. RSW antennas also show promise for array applications, where the usual presence of surface and lateral waves can produce significant mutual-coupling effects.

In this paper, we will consider the shorted annular ring reduced surface-wave (SAR-RSW) antenna. However, the analysis is general and the results we will present are applicable to the general class of RSW antennas introduced in [1]. The properties of the single element SAR-RSW antenna, shown in Fig. 1, have been investigated extensively [1], [2]. In the following sections we will summarize our study of the mutual coupling between pairs of SAR-RSW antennas and present numerical results from a theoretical analysis of the mutual coupling along with confirming experimental results. A numerical study of both the radiation-field and surface-wave contributions to the coupling will be performed to investigate their relative importance, for the case of a typical substrate thickness of approximately 0.01 λ_0. In addition, the mutual coupling behavior will be examined using an asymptotic analysis, which demonstrates how the coupling varies with patch separation.

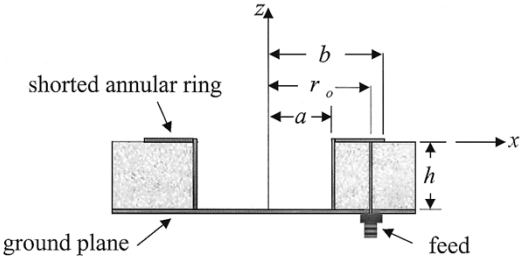

Fig. 1. Shorted annular ring reduced surface-wave (SAR-RSW) antenna.

II. Shorted Annular Ring Reduced Surface-Wave Antennas

The vertical component of the electric field along the ground plane for the TM_0 surface wave excited by an equivalent edge magnetic current $K_\varphi = \cos\varphi$ corresponding to the TM_{011} mode of a circular patch antenna is given by [1]

$$E_z^{\mathrm{SW}} \approx BH_1^{(2)}(k_{\mathrm{TM}_0}\rho)\cos(\varphi)J_1'(k_{\mathrm{TM}_0}b) \tag{1}$$

where

k_{TM_0} propagation wavenumber for the TM_0 surface wave;
b radius of the patch;
B constant that depends on the substrate geometry.

From this equation it is apparent that the amplitude of the surface wave will be zero when we choose the radius b such that

$$b = \frac{x_{11}'}{k_{\mathrm{TM}_0}} \tag{2}$$

where x_{11}' is the first zero of $J_1'(x)$. (The first zero is selected to give the smallest possible patch size.) Hence, any circular ring of magnetic current that has a $\cos\varphi$ azimuthal variation and a radius satisfying (2) will not excite the dominant TM_0 surface wave of the grounded dielectric substrate. In addition, if the substrate is electrically thin, then

$$k_{\mathrm{TM}_0} \approx k_o \tag{3}$$

Manuscript received August 31, 1999; revised May 10, 2000.

The authors are with the Department of Electrical and Computer Engineering, University of Houston, Houston, TX 77204-4793 USA (e-mail: jwilliams@uh.edu).

Publisher Item Identifier S 0018-926X(00)09354-6.

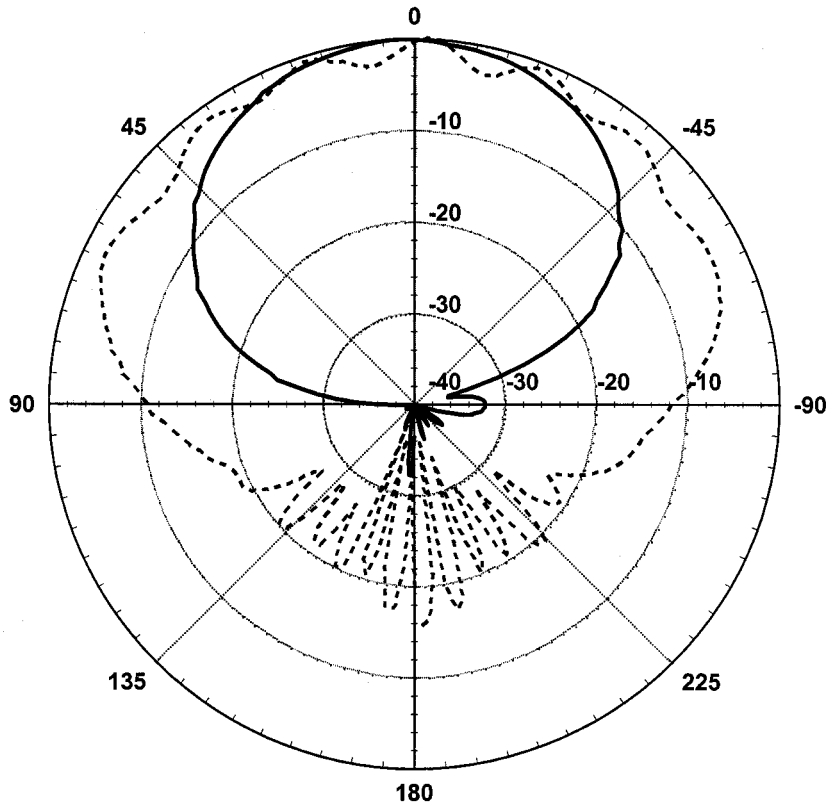

Fig. 2. Measured E-plane radiation patterns for a conventional circular patch (dashed line) and a SAR-RSW antenna (solid line) on a 1-m-diameter circular ground plane.

where k_o is the free-space propagation wavenumber. This suggests that RSW patch on a thin substrate will also have reduced lateral-wave excitation, since the lateral wave propagates with a wavenumber k_o. Equation (3) also suggests that the radius b obtained from (2) is nearly independent of the permittivity for electrically thin substrates.

For the SAR-RSW antenna, the outer radius is selected to satisfy the RSW condition given by (2). The radius a of the short-circuit inner boundary is then selected to make the antenna resonate at the RSW design frequency. This is accomplished by selecting an inner radius that satisfies the following transcendental equation [1]

$$\frac{J_1(k_1 a)}{Y_1(k_1 a)} = \frac{J_1'\left(\frac{k_1 x_{11}'}{k_{\mathrm{TM}_0}}\right)}{Y_1'\left(\frac{k_1 x_{11}'}{k_{\mathrm{TM}_0}}\right)} \tag{4}$$

where k_1 is the wavenumber for the dielectric of the substrate. Equation (4) has at least one solution for all values of ε_r and additional solutions as ε_r increases. To get two solutions the relative permittivity of the substrate must be greater than 8.4 [1]. Each of these solutions result in different values of the inner radius a. Since the outer radius b is generally larger than that of a conventional circular patch, the RSW structures are multimoded, with resonances at frequencies above and below that of the RSW mode.

In Fig. 2, we show a comparison of the experimental E-plane radiation patterns for a conventional circular patch and a SAR-RSW patch mounted on a 1-m-diameter circular ground plane at an operating frequency of 2 GHz. The substrate has a relative dielectric constant of 2.94 and a thickness of 0.15 cm. At this operating frequency, the SAR-RSW antenna has an inner radius of 2.42 cm and an outer radius of 4.39 cm. The conventional circular patch antenna has a radius of 2.66 cm. A 50-Ω coaxial probe is used to feed both antennas at their respective match points.

In Fig. 2, we immediately notice that the RSW antenna is more directive, and also radiates very little power along the horizon. As a result there is little power diffracted to the backside of the ground plane. The significant scalloping on the front side and strong field levels on the backside for the conventional patch are due to the edge diffraction of the strong fields radiated along the horizon in the E-plane of this antenna. Fig. 3 shows a comparison of the experimental H-plane radiation patterns for the two antennas. We observe that the two patterns are nearly identical except that the conventional circular patch has a strong, yet narrow, backside lobe at $\theta = 180°$. This is due to the fact that at this angle diffraction from the entire edge of the circular ground plane contributes to the H-pattern. Hence, strong E-plane diffraction affects the H-plane pattern of the conventional patch at $\theta = 180°$ (and also $\theta = 0°$, where a bump in the pattern is visible). For the SAR-RSW antenna, this back-

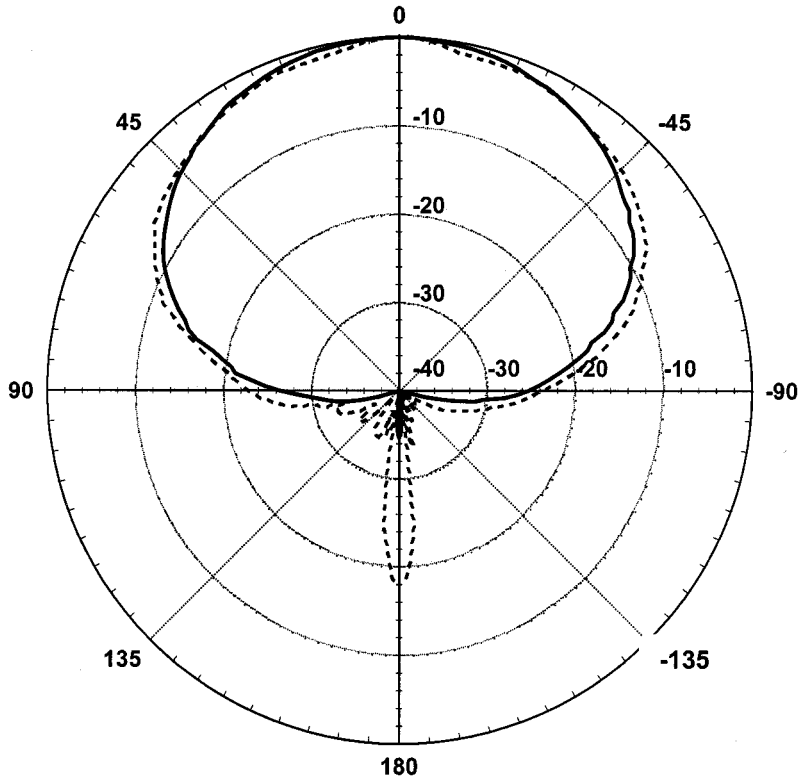

Fig. 3. Measured H-plane radiation patterns for a conventional circular patch (dashed line) and a SAR-RSW antenna (solid line) on a 1-m-diameter circular ground plane.

side lobe has been significantly reduced and the pattern lacks the characteristic diffraction bump at $\theta = 0°$.

Clearly, the radiation patterns demonstrate that the RSW antennas produce less fields along the horizon than do conventional microstrip antennas. It is natural to therefore investigate whether this translates into a reduced mutual coupling between RSW antennas, compared to conventional microstrip antennas. This is explored in the remainder of the paper, where the mutual coupling between RSW antennas is obtained both numerically and experimentally, and the nature of the mutual coupling is investigated.

For all of the experimental results presented in this paper, the conventional circular patch and the SAR-RSW antennas are designed to operate at a frequency of 2 GHz, with the same substrate and antenna parameters as in Fig. 2. The thickness of this substrate is approximately 0.01 λ_0.

III. Mutual Coupling

A. Theoretical Analysis

The geometry used in the calculation of the mutual coupling between two identical antennas is shown in Fig. 4. In order to obtain an expression for the mutual coupling, we model the two antennas as a general two-port network, where the mutual impedance is written as

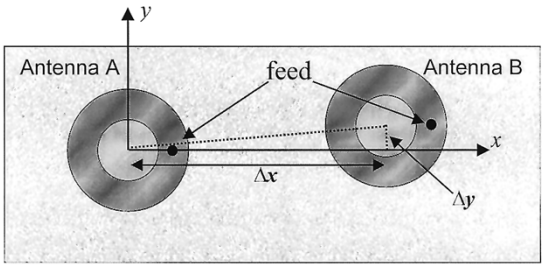

Fig. 4. Geometry used in the calculation of the mutual coupling between two conventional circular microstrip patch antennas and two SAR-RSW antennas.

$$Z_{12} = \left.\frac{V_1}{I_2}\right|_{I_1=0} \tag{5}$$

where V_1 is the open-circuit voltage at feed port 1 due to a current I_2 that is applied to feed port 2. Referring to Fig. 4, port 1 is connected to antenna A and port 2 to Antenna B. By using the equivalence principle in conjunction with the reciprocity theorem [7] we write (5) as

$$Z_{12} = \frac{1}{I_1 I_2} \int_{S_A} \vec{H}\left[\vec{M}_s^B\right] \cdot \vec{M}_s^A \, ds \tag{6}$$

where $\vec{M}_S^B$ is the equivalent sheet of magnetic current at the edge(s) of antenna B with a feed current I_2 and $\vec{M}_S^A$ is the sheet of magnetic current at the edge(s) of antenna A with a feed current I_1. Note that the square brackets in (6) indicate that we are calculating the magnetic field due to the magnetic current sheet $\vec{M}_S^B$. For thin substrates ($h \ll \lambda_0$), the sheets of magnetic current are well approximated by rings of magnetic current located at the center of the substrate. Setting $I_1 = I_2 = 1$, the expressions for these equivalent magnetic current rings, are given as

$$K_\varphi^A = h \sum_{m=0}^{\infty} A_m \cos(m\varphi^A) \tag{7}$$

and

$$K_\varphi^B = h \sum_{n=0}^{\infty} A_n \cos(n\varphi^B). \tag{8}$$

The terms A_m and A_n correspond to the amplitude of the modal magnetic surface currents densities (electric fields at the edges of the patches) for modes m and n on antennas A and B, respectively. The thickness of the substrate is denoted by h, and φ^A, φ^B denote local polar coordinates on the two patches. The electric fields at the edges of the patches were calculated using the cavity model [8]. In this model the edge conductance was determined using a spectral-domain calculation of the power radiated by the magnetic current ring, including space-wave and surface-wave power [9].

Using (7) and (8) the mutual impedance in (6) is written as

$$Z_{12} = -h^2 \sum_{m=0}^{\infty} \sum_{n=0}^{\infty} A_m A_n R_{mn} \tag{9}$$

where

$$R_{mn} = -\int_0^{2\pi} H_\varphi[\cos(n\varphi^B)] \cos(m\varphi^A) b \, d\varphi^A \tag{10}$$

and b is the outer radius of antenna A. In (10), R_{mn} represents the reaction between two unit strength rings of magnetic current. As derived in the Appendix, the final expression for (10) is given by

$$R_{mn} = R_{mn}^{\mathrm{TE}} + R_{mn}^{\mathrm{TM}} \tag{11}$$

where

$$\begin{aligned} R_{mn}^{\mathrm{TE}} = {} & \pi(-j)^{m-1} j^{n-1} mn (k_o b)^2 \int_0^{\infty} \\ & \cdot I_v^{\mathrm{TE}}(\beta) \left[\frac{J_m(k_o\beta b)}{k_o\beta b}\right] \left[\frac{J_n(k_o\beta b)}{k_o\beta b}\right] \\ & \cdot \{j^{n-m} \cos[(n-m)\alpha] J_{n-m}(2\pi\beta\gamma) - j^{n+m} \\ & \cdot \cos[(n+m)\alpha] J_{n+m}(2\pi\beta\gamma)\} \beta \, d\beta \end{aligned} \tag{12}$$

$$\begin{aligned} R_{mn}^{\mathrm{TM}} = {} & \pi(-j)^{m-1} j^{n-1} (k_o b)^2 \int_0^{\infty} \\ & \cdot I_v^{\mathrm{TM}}(\beta) J_m'(k_o\beta b) J_n'(k_o\beta b) \\ & \cdot \{j^{n-m} \cos[(n-m)\alpha] J_{n-m}(2\pi\beta\gamma) + j^{n+m} \\ & \cdot \cos[(n+m)\alpha] J_{n+m}(2\pi\beta\gamma)\} \beta \, d\beta \end{aligned} \tag{13}$$

$$\alpha = \tan^{-1}\left(\frac{\Delta y}{\Delta x}\right) \tag{14}$$

$$\gamma = \Delta\overline{x}\cos\alpha + \Delta\overline{y}\sin\alpha \tag{15}$$

$\Delta\overline{x} = \Delta x/\lambda_o$, $\Delta\overline{y} = \Delta y/\lambda_o$, and $\beta = k_\rho/k_o$. Referring to Fig. 4, Δx and Δy are the center-to-center patch separations in the x and y directions. In this work we will consider patches separated along the E-, D-, and H-planes, which correspond to $\Delta y = 0$, $\Delta x = \Delta y$, and $\Delta x = 0$, respectively. The functions I_v^{TM} and I_v^{TE} are the currents obtained from a spectral-domain transmission line analysis of the background structure [10]. In particular, these currents correspond to the currents at $z = h/2$ in the TM and TE transmission line models, due to a 1-V series feed at the same location. They are given by

$$\begin{aligned} & I_v^{\mathrm{TM}}(k_\rho) \\ & = \frac{Z_1^{\mathrm{TM}} + jZ_o^{\mathrm{TM}} \tan\left(\frac{k_z h}{2}\right)}{Z_o^{\mathrm{TM}} Z_1^{\mathrm{TM}} \left[1 - \tan^2\left(\frac{k_z h}{2}\right)\right] + j2(Z_1^{\mathrm{TM}})^2 \tan\left(\frac{k_z h}{2}\right)} \end{aligned} \tag{16}$$

and

$$\begin{aligned} & I_v^{\mathrm{TE}}(k_\rho) \\ & = \frac{Z_1^{\mathrm{TE}} + jZ_o^{\mathrm{TE}} \tan\left(\frac{k_z h}{2}\right)}{Z_o^{\mathrm{TE}} Z_1^{\mathrm{TE}} \left[1 - \tan^2\left(\frac{k_z h}{2}\right)\right] + j2(Z_1^{\mathrm{TE}})^2 \tan\left(\frac{k_z h}{2}\right)} \end{aligned} \tag{17}$$

where

$$Z_o^{\mathrm{TM}} = \frac{\sqrt{k_o^2 - k_\rho^2}}{\omega\varepsilon_o} \tag{18}$$

$$Z_1^{\mathrm{TM}} = \frac{\sqrt{\varepsilon_r k_o^2 - k_\rho^2}}{\omega\varepsilon_r\varepsilon_o} \tag{19}$$

$$Z_o^{\mathrm{TE}} = \frac{\omega\mu_o}{\sqrt{k_o^2 - k_\rho^2}} \tag{20}$$

$$Z_1^{\mathrm{TE}} = \frac{\omega\mu_o}{\sqrt{\varepsilon_r k_o^2 - k_\rho^2}}. \tag{21}$$

The integrals in (12) and (13) are evaluated numerically using a Sommerfeld contour that detours above the surface-wave pole located at $\beta = k_{\mathrm{TM}_0}/k_0$ and the branch point located at $\beta = 1$. Numerically, this contour was implemented as a path, starting at the origin, which initially follows a rectangle in the complex β plane, of height 0.05 and width $1.5\sqrt{\varepsilon_r}$. The path then proceeds along the real axis to a value of $100\sqrt{\varepsilon_r}$, which was sufficient to obtain convergence for the antennas in this study.

Once the mutual impedance has been obtained, the S_{12} scattering parameter is calculated using

$$|S_{12}|^{\mathrm{dB}} = 20\log_{10}\left|\frac{2Z_o Z_{12}}{(Z_{11}+Z_o)^2 - Z_{12}^2}\right| \tag{22}$$

where we typically assume $Z_{11} = Z_o = 50\ \Omega$. For the remainder of this work we will refer to $|S_{12}|$ as the coupling magnitude.

B. Comparison of Theoretical and Measured Mutual Coupling

In this section, we will compare the mutual coupling theory from the previous section with experimental results. Since the conventional circular microstrip patch has been extensively studied in the past, we will first compare our theoretical results for the mutual coupling between a pair of circular patch antennas with E-plane and H-plane measurements obtained from [11]. These antennas have a radius of 0.93 cm, a substrate thickness of 0.15 cm, and a dielectric constant of 2.64. In [11], data is not given for the conductivity of the copper, the dielectric loss tangent, or the radius of the feed pin. Therefore, we chose values of 3×10^7 S/m for the conductivity, 0.0012 for the dielectric loss tangent and 0.0625 cm for the radius of the feed pin. The radius of the feed pin is that of a 50-Ω coaxial SMA probe. Note that because of surface roughness, the effective conductivity of the copper patches and ground plane was chosen to be less than that of pure bulk copper (5.8×10^7 S/m). This data is used specifically in the calculation of the input impedance [2]. As a result, the match point is located at a radius of 0.23 cm from the center of the patch and the resonant frequency is 5.369 GHz. Although the mutual impedance expression in (9) contains the sum over all possible cavity modes for each of the antennas, the first 16 combinations (four modes on each patch) were found to be sufficient to accurately compute the mutual coupling for all the cases we have considered. The theoretical results for the mutual coupling versus the center-to-center separation are plotted with the measured data in Fig. 5. Notice that there is good agreement for both E-plane and H-plane coupling. The slightly lower values measured for the E-plane coupling are probably due to scattering within the local environment of the measurement and possible mismatches between the antennas tested.

We will now compare our mutual coupling theory with a set of carefully measured results we obtained for the E-plane mutual coupling between a pair of conventional circular microstrip patches and a pair of SAR-RSW antennas. Both sets of antennas were fabricated using Rogers RT/duroid 6002 double-sided copper clad substrates. Standard ultraviolet lithography and chemical etching techniques were used to fabricate the SAR-RSW antennas and the conventional circular patch antennas. The design of the antennas and physical properties of the substrate have been discussed in Section II. The antennas were attached to a supporting ground plane that allowed us to obtain a maximum center-to-center separation of approximately four wavelengths for a design frequency of 2 GHz.

For ideal mutual coupling measurements, the two antennas should be perfectly matched and resonant at the same frequency. This, of course, is difficult to achieve in practice. For this reason, practical restraints were placed on the relative operation of the two antennas. In our measurements, the input reflection coefficient for each antenna was kept below -20 dB and the operating frequency of each of the two antennas was kept within the other's 2 : 1 VSWR bandwidth. To avoid effects from scattering within the measurement environment, the test structure was mounted inside the throat of a 27-ft tapered anechoic chamber.

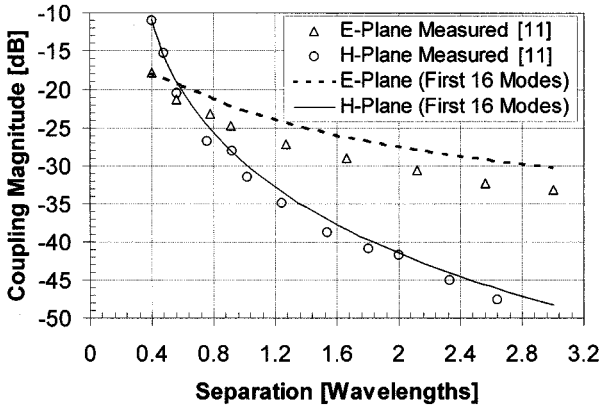

Fig. 5. E-plane and H-plane mutual coupling results for the conventional circular microstrip patch antenna.

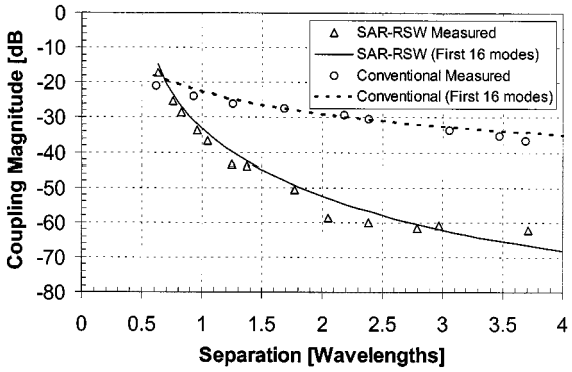

Fig. 6. E-plane mutual coupling for conventional circular microstrip patch antennas 1 SAR-RSW antennas.

The results for the E-plane mutual coupling between conventional circular microstrip patch antennas and SAR-RSW antennas versus separation are shown in Fig. 6. For both sets of antennas there is excellent agreement between the theory and the measurement. Some deviation occurs for distances greater than three wavelengths. This is probably due to the fact that at these separations the antennas are relatively close to the edge of the supporting ground plane. It is important to note that the edges of the conventional circular microstrip patch are touching at a separation of approximately 0.4 wavelengths, while the SAR-RSW antennas are touching at approximately 0.6 wavelengths.

We observe in Fig. 6 that the E-plane mutual coupling between SAR-RSW antennas decreases much more rapidly with separation than that for conventional circular microstrip antennas. This is in agreement with the radiation patterns of Section II, which showed a much lower field level radiated from the antenna along the interface. A detailed investigation of this mutual coupling behavior will be given in the following sections, in order to determine the radiation mechanism that is primarily responsible for the mutual coupling.

C. Modal Contributions to the Mutual Coupling

In this section, we show that the mutual coupling between adjacent elements is predominately due to the dominant mode

of each antenna ($m = 1$ and $n = 1$). This is demonstrated for the E-plane case, which is the case with the largest coupling. The dominant-mode coupling versus the mutual coupling calculated using the first 16 mode combinations (four modes on each patch, $m \leq 4$ and $n \leq 4$) for the conventional circular microstrip patch antenna is shown in Fig. 7. From these results, we observe that for patch separations up to at least ten wavelengths, the mutual coupling between conventional microstrip patches is accurately predicted by using only the dominant mode contribution.

By design, the dominant mode magnetic current of the SAR-RSW antenna does not excite any surface waves. Therefore, it is not readily apparent whether or not the higher order modes will be needed when calculating the mutual coupling for these antennas. In Fig. 8 we compare the mutual coupling between SAR-RSW antennas calculated using only the dominant mode and calculated using the first 16 mode combinations. It is seen that the higher order modes have more of an effect as compared to the conventional circular microstrip patch antenna. However, below approximately three to four wavelengths separation the dominant mode is still sufficient to accurately predict the mutual coupling between SAR-RSW antennas. This is an indication that for these separations the majority of the mutual coupling is not due to the surface wave, a fact that will be verified in the next section.

From (9)–(13) the mutual impedance due to the dominant mode of each patch can be written as

$$Z_{12} = -h^2 A_1^2 (R_{11}^{\mathrm{TE}} + R_{11}^{\mathrm{TM}}) \tag{23}$$

where

$$R_{11}^{\mathrm{TE}} = \pi (k_o b)^2 \int_0^\infty I_v^{\mathrm{TE}} \left[\frac{J_1(k_o \beta b)}{k_o \beta b} \right]^2 \cdot \{ J_0(2\pi\beta\gamma) + \cos[2\alpha] J_2(2\pi\beta\gamma) \} \beta \, d\beta \tag{24}$$

and

$$R_{11}^{\mathrm{TM}} = \pi (k_o b)^2 \int_0^\infty I_v^{\mathrm{TM}} [J_1'(k_o \beta b)]^2 \cdot \{ J_0(2\pi\beta\gamma) - \cos[2\alpha] J_2(2\pi\beta\gamma) \} \beta \, d\beta. \tag{25}$$

Fig. 9 shows theoretical plots for the E-plane, H-plane, and D-plane mutual coupling for both conventional and RSW antennas, based on dominant-mode coupling. Interestingly, for the SAR-RSW antenna the H-plane exhibits the strongest coupling for patch separations greater than approximately one wavelength, as opposed to the E-plane for the conventional circular microstrip patch antenna. For the SAR-RSW antenna, the lowest coupling magnitude for separations between 0.6–0.8 wavelengths is in the H-plane. Between 0.8–1.5 wavelengths, the lowest coupling is in the D-plane and, for greater separations, the E-plane mutual coupling is the smallest.

IV. Physical Contributions to the Mutual Coupling

In this section, we will analyze the conventional microstrip patch antenna to determine the physical radiation mechanism that is primarily responsible for the mutual coupling. This will provide insight into the mutual coupling and help explain why it is reduced for the SAR-RSW antennas. First, some background information on the physics of radiation from sources in layered media such as microstrip is reviewed in order to define the terminology and aid in the subsequent discussion.

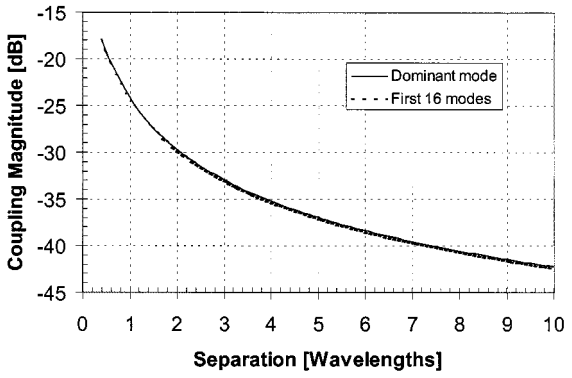

Fig. 7. E-plane mutual coupling between conventional circular microstrip patch antennas calculated using only the dominant mode and calculated using the first 16 modes.

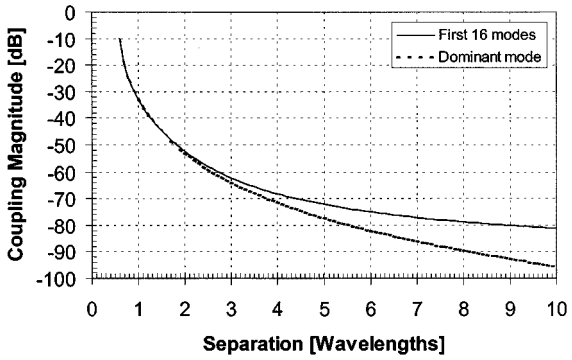

Fig. 8. E-plane mutual coupling between SAR-RSW antennas calculated using only the dominant mode and calculated using the first 16 modes.

A typical microstrip patch antenna (or any other type of microstrip source) will excite one or more surface wave modes as well as a "continuous-spectrum" field, also denoted as the radiation field [5]. Assuming that only the TM_0 surface wave mode is above cutoff, the surface-wave field along the interface will propagate with a wavenumber β_{TM_0} and will decay radially from the antenna as $1/\sqrt{\rho}$ (ρ is the horizontal distance away from the axis of the antenna).

For observation angles (measured from the z axis) less than 90°, the surface-wave field becomes negligible and the radiation field asymptotically evolves into the space-wave field, which is the usual far-field of the microstrip antenna. This field varies as $1/r$ (r is the radial distance away from the antenna) and propagates outward with a wavenumber of k_o.

Along the air-dielectric interface, the radiation field asymptotically evolves into a field that propagates with a wavenumber k_o, but decays with distance along the interface as $1/\rho^2$ (instead of $1/r$). This field is referred to as the lateral-wave field. Hence, far away from a microstrip source, the field along the interface will consist of two parts: a surface-wave field that decays as $1/\sqrt{\rho}$ and a lateral-wave field that decays as $1/\rho^2$. At extreme distances, the surface-wave field will be dominant.

For thin substrates, the amplitude of the surface-wave mode excited by a microstrip antenna is small; thus, the surface-wave field is fairly weak compared to the radiation field for small or

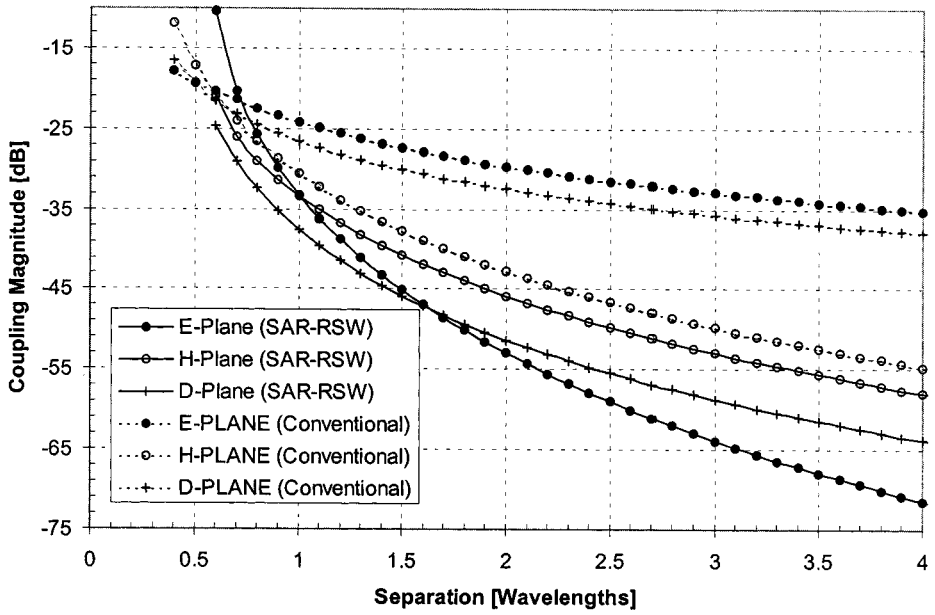

Fig. 9. Dominant mode mutual coupling for the conventional circular microstrip patch and SAR-RSW antenna.

moderate distances from the antenna. Furthermore, when the substrate is thin, the radiation field for small or moderate distances will closely resemble a space-wave type of field, decaying as $1/\rho$ along the interface. Eventually the radiation field along the interface will transition into the lateral-wave field, varying as $1/\rho^2$; however, this transition occurs at large distances when the substrate is thin (in the limit of a vanishingly thin substrate, the radiation field remains a space-wave field for all distances).

The spectral-domain method provides a convenient means to quantify the different contributions to the mutual coupling. Fig. 10 shows a general Sommerfeld path that defines the contour of integration used in the spectral-domain integrals for mutual coupling. When integrating along this path the total mutual coupling, which includes the continuous spectrum (i.e., radiation field) and surface-wave contributions, is obtained. In order to calculate these two effects separately, the integration path is deformed to an integration around the branch cut and an integration around the surface-wave pole, as also shown in Fig. 10. Once this has been done, residue calculus is applied to calculate the mutual coupling associated with the surface wave. The mutual coupling due to the radiation field can be found by integrating around the branch cut, or alternatively, by subtracting the surface-wave contribution from the total mutual coupling. When the observation point is along the interface, far away from the source, the branch-cut integration reduces asymptotically to the branch-point contribution, which yields the lateral wave discussed above [5]. We will consider the dominant-mode E-plane coupling in the detailed analysis that follows.

From (23)–(25) we note that the mutual coupling is determined by separately calculating the TE and TM components. In the calculation of the surface-wave contribution to the mutual coupling the TE component can be neglected since the corresponding integrand does not contain the (TM_0) surface-wave

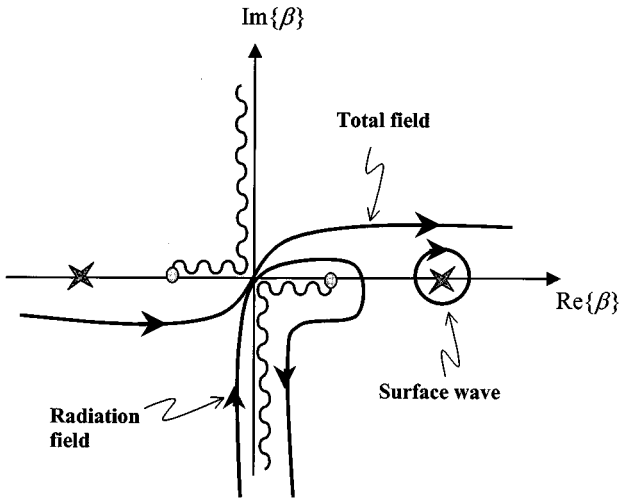

Fig. 10. Integration paths used in the calculation of the mutual coupling.

pole. To be able to deform the path, the limits of the integrand in (25) must extend over the range $(-\infty, \infty)$. Using Bessel function identities and noting that I_v^{TM} is an even function with respect to β allows us to write

$$R_{11}^{\mathrm{TM}} = \pi(k_o b)^2 \int_{-\infty}^{\infty} I_v^{\mathrm{TM}}(\beta)[J_1'(k_o\beta b)]^2 \cdot H_1^{(2)'}(2\pi\beta\Delta\overline{x})\beta\, d\beta. \tag{26}$$

The integration path has now been transformed into the path shown in Fig. 10. (The branch cut along the negative real axis associated with the Hankel function has been omitted from this diagram.) Using Cauchy's integral theorem, this path is deformed to the path around the lower branch cut and the path surrounding

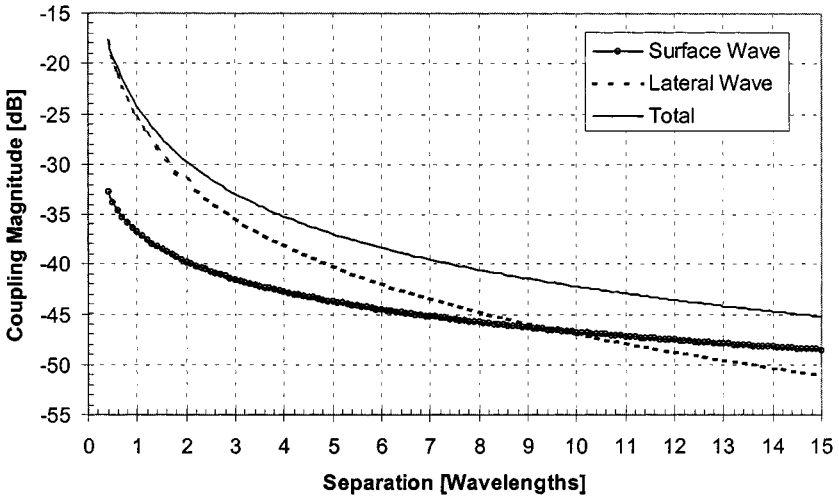

Fig. 11. Different components of the dominant mode E-plane mutual coupling between conventional circular microstrip patch antennas.

the surface-wave pole. From residue calculus, the surface-wave pole contribution to the reaction integral (26) is

$$R_{11}^{\mathrm{TM}} = \pi(k_o b)^2 \left[-2\pi j \mathrm{Res}\left\{I_v^{\mathrm{TM}}\left(\overline{k}_{\mathrm{TM}_0}\right)\right\}\right] \left[J_1'\left(k_o \overline{k}_{\mathrm{TM}_0} b\right)\right]^2 \cdot H_1^{(2)'}\left(2\pi \overline{k}_{\mathrm{TM}_0} \Delta\overline{x}\right) \overline{k}_{\mathrm{TM}_0} \quad (27)$$

where $\overline{k}_{\mathrm{TM}_0} = k_{\mathrm{TM}_0}/k_o$ is the normalized location of the surface-wave pole, which was found numerically to exist at $\overline{k}_{\mathrm{TM}_0} = 1.000\,77$ for the substrate parameters given in Section II. From (23) we write the surface-wave contribution to the mutual impedance as

$$Z_{12}^{\mathrm{SW}} = -h^2 A_1^2 \pi(k_o b)^2 \left[-2\pi j \mathrm{Res}\left\{I_v^{\mathrm{TM}}\left(\overline{k}_{\mathrm{TM}_0}\right)\right\}\right] \cdot \left[J_1'\left(k_o \overline{k}_{\mathrm{TM}_0} b\right)\right]^2 H_1^{(2)'}\left(2\pi \overline{k}_{\mathrm{TM}_0} \Delta\overline{x}\right) \overline{k}_{\mathrm{TM}_0}. \quad (28)$$

The residue in (28) is calculated using

$$\mathrm{Res}\left\{I_v^{\mathrm{TM}}\left(\overline{k}_{\mathrm{TM}_0}\right)\right\} = \frac{N\left(\overline{k}_{\mathrm{TM}_0}\right)}{D'\left(\overline{k}_{\mathrm{TM}_0}\right)} \quad (29)$$

where $N(\overline{k}_{\mathrm{TM}_0})$ represents the numerator of (16) evaluated at $\beta = \overline{k}_{\mathrm{TM}_0}$ and $D'(\overline{k}_{\mathrm{TM}_0})$ is the derivative of the denominator in (16) with respect to β evaluated at $\beta = \overline{k}_{\mathrm{TM}_0}$. The derivative in (29) is written as

$$D'\left(\overline{k}_{\mathrm{TM}_0}\right) = D_1' + D_2' + D_3' \quad (30)$$

where

$$D_1' = -\frac{\overline{k}_{\mathrm{TM}_0}\eta_o^2}{\varepsilon_r}\left[\frac{k_{z1}}{k_{zo}} + \frac{k_{zo}}{k_{z1}}\right] \quad (31)$$

$$D_2' = \frac{\overline{k}_{\mathrm{TM}_0}\eta_o^2}{\varepsilon_r}\left[\left(\frac{k_{z1}}{k_{zo}} + \frac{k_{zo}}{k_{z1}}\right)\tan^2\left(\frac{k_z h}{2}\right) + h k_{zo}\tan\left(\frac{k_z h}{2}\right)\sec^2\left(\frac{k_z h}{2}\right)\right] \quad (32)$$

and

$$D_3' = -\frac{j4\overline{k}_{\mathrm{TM}_0}\eta_o^2}{\varepsilon_r}\left[\tan\left(\frac{k_z h}{2}\right) + \frac{k_z h}{4}\sec^2\left(\frac{k_z h}{2}\right)\right]. \quad (33)$$

Plots of the total E-plane mutual coupling between a pair of conventional circular microstrip patch antennas, with the radiation field and surface-wave contributions shown separately, are given in Fig. 11. For this thin substrate example ($h/\lambda_0 = 0.01$), the mutual coupling is dominated by the radiation-field component up to a separation of approximately seven to eight wavelengths. The surface wave does not dominate the behavior until the separation is greater than approximately ten wavelengths. For the SAR-RSW antenna the surface-wave contribution to the mutual coupling is even less since (by design) the magnetic current of the dominant mode does not excite the surface wave. Hence, for both antennas the majority of the coupling is due to the radiation field, for moderate separations.

V. Asymptotic Analysis of the Mutual Coupling

An asymptotic analysis can be used to explain the behavior of the mutual coupling results shown in Figs. 6 and 9. In the previous section we demonstrated that the radiaton field is the dominant coupling mechanism for patches on thin substrates. Therefore, in an asymptotic analysis of the mutual impedance formula (23), we will neglect the surface-wave contribution. We will begin by outlining the general asymptotic procedure followed by a detailed analysis for the E-plane coupling due to the TM contribution in (23). A summary of the final results for the asymptotic behavior for the E- and H-plane mutual coupling (dominated by TM and TE contributions, respectively) is presented at the end of this section.

Referring to (23), the mutual impedance can be written as

$$Z_{12} = Z_{12}^{\mathrm{TE}} + Z_{12}^{\mathrm{TM}} \quad (34)$$

where $Z_{12}^{\mathrm{TE}} = -h^2 A_1^2 R_{11}^{\mathrm{TE}}$ and $Z_{12}^{\mathrm{TM}} = -h^2 A_1^2 R_{11}^{\mathrm{TM}}$. In general, each term in (34) has the following form:

$$Z_{12}^{i} = \int_{-\infty}^{\infty} f^i(k_\rho, \Delta)\, dk_\rho \quad (35)$$

where $i =$ TE, TM. As the separation Δ between the patches (Δ_x or Δ_y for E- or H-plane coupling) becomes large, an asymptotic expansion of $f^i(k_\rho, \Delta)$ (obtained by asymptotically

approximating the Bessel function terms in the integrand) yields the form

$$Z_{12}^{i} \sim \frac{C}{\Delta^{p_i}} \int_{-\infty}^{\infty} F^{i}(k_\rho) e^{-jk_\rho \Delta}\, dk_\rho \tag{36}$$

where C is a constant and p_i is an exponent that depends on the particular case (TM or TE), as well as the coupling plane (i.e., E-plane, H-plane, or D-plane).

We now deform the path of integration in (36) to the extreme steepest descent path (for observation along the horizon), as shown in Fig. 12. Making the change of variable $k_\rho = k_o - jS$ and neglecting the surface-wave pole, as well as any leaky-wave poles captured by the path deformation, the branch-cut integration (radiation-field contribution) is put in the form

$$Z_{12}^{i} \sim \frac{C}{\Delta^{p_i}} e^{-jk_o\Delta} \int_{0}^{\infty} G^{i}(S) e^{-S\Delta}\, dS \tag{37}$$

where $G^{i}(S) = -j[F_{+}^{i}(k_o - jS) - F_{-}^{i}(k_o - jS)]$. The positive subscript in $F_{+}^{i}(k_o - jS)$ indicates that we are integrating the function on the top (proper) Riemann sheet, while the negative subscript in $F_{-}^{i}(k_o - jS)$ indicates that we are integrating on the bottom (improper) sheet. For a given antenna and substrate geometry, $G^{i}(S)$ can be approximated as

$$G^{i}(S) \sim AS^{\xi_i}, \qquad \text{as } S \to 0 \tag{38}$$

where A is a constant and ξ_i is another exponent that depends on the case considered (TE or TM). Hence, for large Δ (37) becomes

$$Z_{12}^{i} \sim \frac{C}{\Delta^{p_i}} e^{-jk_o\Delta} \int_{0}^{\infty} AS^{\xi_i} e^{-S\Delta}\, dS. \tag{39}$$

Applying Watson's lemma [12] to (39) yields

$$Z_{12}^{i} \sim \frac{C}{\Delta^{p_i}} e^{-jk_o\Delta} \left[\frac{A\Gamma(\xi_i + 1)}{\Delta^{\xi_i+1}}\right] \propto \frac{e^{-jk_o\Delta}}{\Delta^{p_i+\xi_i+1}}. \tag{40}$$

Equation (40) is the final result from the general asymptotic analysis.

Following this general approach we will now detail the asymptotic analysis for the specific cases of the E-plane mutual coupling for conventional circular microstrip patches and SAR-RSW antennas, due to the TM contribution. As we will show, the TM part is the dominant contributor to the E-plane coupling. By noting that $k_\rho = k_o\beta$, the TM component of (23) is given by

$$Z_{12}^{\mathrm{TM}} = -hA_1^2\pi b^2 \int_{-\infty}^{\infty} I_v^{\mathrm{TM}}(k_\rho)[J_1'(k_\rho b)]^2 \cdot H_1^{(2)'}(k_\rho \Delta x) k_\rho\, dk_\rho. \tag{41}$$

Neglecting higher order Δx terms, the asymptotic expansion for the Hankel function in (41) is written as [13]

$$H_1^{(2)'}(k_\rho\Delta x) \sim -je^{j(3/4)\pi}\sqrt{\frac{2}{\pi k_\rho \Delta x}} e^{-jk_\rho\Delta x}. \tag{42}$$

Substituting this into (41) yields

$$Z_{12}^{\mathrm{TM}} \sim hA_1^2 je^{j(3/4)\pi}\pi b^2 \int_{-\infty}^{\infty} I_v^{\mathrm{TM}}(k_\rho)\sqrt{\frac{2}{\pi k_\rho \Delta x}} \cdot [J_1'(k_\rho b)]^2 e^{-jk_\rho\Delta x} k_\rho\, dk_\rho. \tag{43}$$

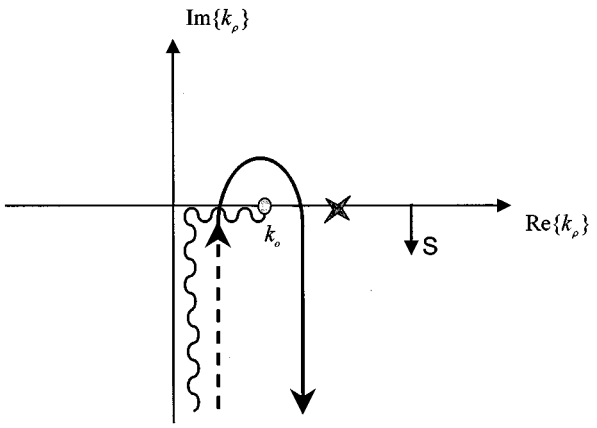

Fig. 12. Steepest-descent path used in the asymptotic analysis of the mutual coupling. The dashed line is used to indicate the lower (improper) sheet of the Reimann surface, while the solid line represents the upper (proper) sheet.

Denoting

$$F^{\mathrm{TM}}(k_\rho) = hA_1^2\sqrt{\frac{2}{\pi k_\rho}}[J_1'(k_\rho b)]^2 I_v^{\mathrm{TM}}(k_\rho) j e^{j(3/4)\pi}\pi b^2 k_\rho \tag{44}$$

we write

$$Z_{12}^{\mathrm{TM}} \sim \frac{1}{\sqrt{\Delta x}} \int_{-\infty}^{\infty} F^{\mathrm{TM}}(k_\rho) e^{-jk_\rho\Delta x}\, dk_\rho. \tag{45}$$

Deforming the integration path to the path of steepest descent allows us to write (45) as

$$Z_{12}^{\mathrm{TM}} \sim \frac{e^{-jk_o\Delta x}}{\sqrt{\Delta x}} \int_{0}^{\infty} G^{\mathrm{TM}}(S) e^{-S\Delta x}\, dS. \tag{46}$$

Using the approximation in (38) yields

$$Z_{12}^{\mathrm{TM}} \sim \frac{e^{-jk_o\Delta x}}{\sqrt{\Delta x}} \int_{0}^{\infty} AS^{\xi} e^{-S\Delta x}\, dS. \tag{47}$$

Applying Watson's lemma to (47) gives us the result

$$Z_{12}^{\mathrm{TM}} \sim \frac{A\Gamma(\xi+1)e^{-jk_o\Delta x}}{\sqrt{\Delta x}(\Delta x^{\xi+1})} \propto \frac{e^{-jk_o\Delta x}}{\Delta x^{\xi+3/2}}. \tag{48}$$

This is the final expression we need to analyze the asymptotic behavior for the TM, E-plane mutual coupling. Comparing (48) with (40) we can immediately determine that $p = 1/2$ for the TM, E-plane case. Further analysis is required to determine the constant A and the value of ξ.

The behavior of $G^{\mathrm{TM}}(S)$ depends on I_v^{TM}. To approximate the I_v^{TM} function for $S \to 0$, it is assumed, for simplicity, that h is vanishingly small. This means that surface-wave and lateral-wave effects are neglected, and only the space-wave field is important for the mutual coupling. A more sophisticated uniform asymptotic analysis, such as that given in [14], would account for the surface wave. From (16) we then have $I_v^{\mathrm{TM}} \approx 1/Z_0^{\mathrm{TM}}$. Using (18) together with $k_\rho = k_o - jS$ results in $I_v^{\mathrm{TM}} \propto S^{-1/2}$ as $S \to 0$. This, in turn, implies that $G^{\mathrm{TM}}(S) \propto S^{-1/2}$ as $S \to 0$; hence, for this case $\xi = -1/2$. Substituting this result into (48) gives the result that the TM, E-plane mutual coupling for the conventional circular microstrip patch antenna has a $1/\Delta x$ behavior as Δx becomes large.

The I_v^{TM} function has the same behavior for the SAR-RSW antenna as it does for the conventional circular microstrip patch antenna, since it does not depend on the antenna geometry. However, there is one very important difference between the two antennas. This difference lies in the $(J_1'[(k_o - jS)b])^2$ term in (44), which is part of the $G^{\mathrm{TM}}(S)$ function in (46). Taking the first two terms of the Taylor series expansion of this Bessel function about $S = 0$ yields

$$J_1'[(k_0 - jS)b] \approx J_1'(k_0 b) + (-jbS)J_1''(k_0 b). \tag{49}$$

By design, $J_1'(k_0 b) = 0$ for the SAR-RSW antenna (assuming $\beta_{\mathrm{TM}_0} \approx k_0$). This is not the case, however, for the conventional circular microstrip patch antenna. The square of the expression in (49) thus yields an S^2 behavior for the SAR-RSW antenna. This result, coupled with the $S^{-1/2}$ behavior of I_v^{TM}, gives the SAR-RSW antenna an overall behavior described by $\xi = 3/2$. Therefore, the TM, E-plane mutual coupling for the SAR-RSW antenna has $1/\Delta x^3$ behavior as Δx gets large.

Following a similar procedure to that described above, the asymptotic behavior for the E-, H-, and D-plane mutual coupling can be determined. The results are summarized in Tables I and II. In Table II, the "Total" asymptotic formula for the coupling comes from considering the slowest decaying component (TE or TM).

A plot of the theoretical and asymptotic E-plane mutual coupling is shown in Fig. 13. As expected, the asymptotic behavior matches the theory as Δx increases. The slight difference between the results for the conventional circular patches for large separations is due to residual surface-wave coupling, which was neglected in the asymptotic analysis. In this figure, the individual asymptotic curves have been normalized to the exact values at 2 λ.

The results in Table II confirm the calculated results in Fig. 9. In particular, Fig. 9 shows that the E-plane coupling falls off much faster with patch separation for the SAR-RSW antennas than for the conventional circular microstrip antennas. However, the H-plane coupling is similar for the conventional and SAR-RSW antennas. The D-plane coupling falls off faster for the SAR-RSW patches.

TABLE I
THE PARAMETERS IN (40) FOR THE MUTUAL COUPLING BETWEEN PAIRS OF CONVENTIONAL CIRCULAR MICROSTRIP PATCHES AND PAIRS OF SAR-RSW ANTENNAS, ASSUMING A THIN SUBSTRATE

		TE	TM
p	**E-plane**	3/2	1/2
	H-plane	1/2	3/2
	D-plane	1/2	1/2
ξ	**Conventional**	1/2	-1/2
	SAR-RSW	1/2	3/2

TABLE II
ASYMPTOTIC BEHAVIOR FOR THE MUTUAL COUPLING BETWEEN PAIRS OF CONVENTIONAL CIRCULAR MICROSTRIP PATCHES AND PAIRS OF SAR-RSW ANTENNAS, ASSUMING A THIN SUBSTRATE (THE MUTUAL COUPLING IS DUE ONLY TO THE SPACE-WAVE FIELD, AND THE SURFACE-WAVE HAS BEEN NEGLECTED)

		TE	TM	TOTAL
E-plane	**Conventional**	$1/\Delta x^3$	$1/\Delta x$	$1/\Delta x$
	SAR-RSW	$1/\Delta x^3$	$1/\Delta x^3$	$1/\Delta x^3$
H-plane	**Conventional**	$1/\Delta y^2$	$1/\Delta y^2$	$1/\Delta y^2$
	SAR-RSW	$1/\Delta y^2$	$1/\Delta y^4$	$1/\Delta y^2$
D-plane	**Conventional**	$1/\Delta^2$	$1/\Delta$	$1/\Delta$
	SAR-RSW	$1/\Delta^2$	$1/\Delta^3$	$1/\Delta^2$

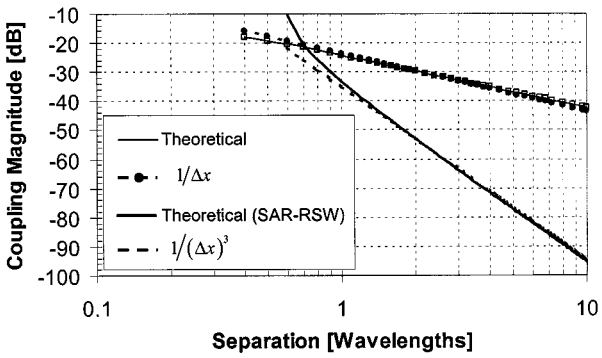

Fig. 13. E-plane mutual coupling for conventional microstrip patches and SAR-RSW antennas.

VI. CONCLUSION

We have investigated the mutual coupling between shorted annular ring reduced surface-wave (SAR-RSW) antennas and compared the behavior with conventional circular microstrip patch antennas. We saw excellent agreement between theory and measurement for both structures. The E- and D-plane mutual coupling was significantly less for the SAR-RSW antennas compared to the conventional circular patch antennas for separations greater than a wavelength.

We then investigated the relative contributions of the surface-wave field and radiation field to the mutual coupling. We showed that for a conventional microstrip antenna on an electrically thin substrate ($h/\lambda_0 \approx 0.01$), the mutual coupling is dominated by the radiation field (continuous spectrum) for small or moderate patch separations. This is also true for the mutual coupling between SAR-RSW antennas. Furthermore, for thin substrates the radiation field along the interface has the character of a space wave (the type of wave that would be radiated by the antenna in free-space, without the substrate). An asymptotic analysis for the mutual coupling based on the space wave was then developed. For relatively large patch separations, the asymptotic analysis accurately predicted a $1/\Delta$ falloff for the E-plane mutual coupling between conventional circular patch antennas and $1/(\Delta)^3$ for the SAR-RSW antennas, where Δ is the center-to-center separation between antennas. In the H-plane the mutual coupling has a $1/(\Delta)^2$ dependence for both antennas. In the D-plane the mutual coupling varies as $1/\Delta$ between conventional circular patches and as $1/\Delta^2$ between

SAR-RSW antennas. Hence, as the patch separation increases the mutual coupling becomes much smaller for SAR-RSW antennas compared to conventional circular patches, in both the E- and D-planes. The mutual coupling is not significantly reduced in the H-plane, but in this plane the mutual coupling is inherently small.

Hence, while the antenna under investigation is referred to as a "reduced surface wave" antenna, the mutual coupling is mainly reduced by virtue of a significant reduction in the space-wave excitation along the interface, at least for thin substrates and moderate patch separations. For larger separations or thicker substrates, the surface wave would become more important, and then a lowering of the mutual coupling would indeed occur through a reduction in the surface-wave excitation.

Appendix
Evaluation of the Reaction Integral

The reaction between two normalized rings of magnetic current is given by

$$R_{mn} = -\int_0^{2\pi} H_\varphi[\cos(n\varphi^B)]\cos(m\varphi^A) b\, d\varphi^A. \tag{A.1}$$

The magnetic field in (A.1) is written as

$$H_\varphi = -H_x \sin\varphi^A + H_y \cos\varphi^A \tag{A.2}$$

which yields

$$R_{mn} = -\int_0^{2\pi} [-H_x \sin\varphi^A + H_y \cos\varphi^A]\cos(m\varphi^A) b\, d\varphi^A. \tag{A.3}$$

Writing H_x and H_y in terms of their Fourier transforms yields

$$H_x = \frac{1}{(2\pi)^2}\int_{-\infty}^{\infty}\int_{-\infty}^{\infty} \tilde{H}_x e^{-j(k_x x + k_y y)}\, dk_x\, dk_y \tag{A.4}$$

and

$$H_y = \frac{1}{(2\pi)^2}\int_{-\infty}^{\infty}\int_{-\infty}^{\infty} \tilde{H}_y e^{-j(k_x x + k_y y)}\, dk_x\, dk_y. \tag{A.5}$$

The spectral domain immitance (SDI) method formulated in [15], [16] will be used to calculate $\tilde{H}_x$ and $\tilde{H}_y$. The fields can be broken into TE and TM components with respect to the direction of propagation by the use of a rotated $u-v$ coordinate system [15], [17], which yields

$$H_x = \frac{1}{(2\pi)^2}\int_0^{\infty}\int_0^{2\pi}\left(\tilde{H}_u\cos\overline{\varphi} - \tilde{H}_v\sin\overline{\varphi}\right) \cdot e^{-jk_\rho b\cos(\overline{\varphi}-\varphi^A)} k_\rho\, d\overline{\varphi}\, dk_\rho \tag{A.6}$$

and

$$H_y = \frac{1}{(2\pi)^2}\int_0^{\infty}\int_0^{2\pi}\left(\tilde{H}_u\sin\overline{\varphi} + \tilde{H}_v\cos\overline{\varphi}\right) \cdot e^{-jk_\rho b\cos(\overline{\varphi}-\varphi^A)} k_\rho\, d\overline{\varphi}\, dk_\rho \tag{A.7}$$

where $\overline{\varphi}$ is the polar angle in the $k_x - k_y$ plane.

In the SDI approach, the TE component of the magnetic field due to a ring of magnetic current, located at the center of the substrate, is given by

$$\tilde{H}_u = I_V^{\mathrm{TE}} V_S^{\mathrm{TE}} \tag{A.8}$$

where I_v^{TE} is defined as the current in the TE equivalent transmission line model due to a series one-volt source at the center of the substrate. The source term V_S^{TE} can be separated into x and y components as

$$V_S^{\mathrm{TE}} = -\left(\tilde{M}_x\cos\overline{\varphi} + \tilde{M}_y\sin\overline{\varphi}\right) \tag{A.9}$$

where $\tilde{M}_x$ and $\tilde{M}_y$ represent the transverse Fourier transforms of the x and y components of the surface current corresponding to the unit-strength magnetic current ring, which is given by

$$\vec{M}_S = \hat{\varphi}\delta(\rho - b)\cos(n\varphi). \tag{A.10}$$

In this expression b is the radius of the current ring and $\delta(\rho - b)$ is the Dirac delta function. From (A.10), we obtain

$$M_x = -\delta(\rho - b)\cos(n\varphi)\sin\varphi \tag{A.11}$$

and

$$M_y = \delta(\rho - b)\cos(n\varphi)\cos\varphi. \tag{A.12}$$

We can write (A.9) as

$$V_S^{\mathrm{TE}} = -\int_{-\infty}^{\infty}\int_{-\infty}^{\infty}(M_x\cos\overline{\varphi} + M_y\sin\overline{\varphi}) \cdot e^{j(k_x x + k_y y)}\, dx\, dy. \tag{A.13}$$

For generality, we will assume that the antenna is located at a relative position $(\Delta x, \Delta y)$ with respect to the origin. Hence, using (A.11) and (A.12), (A.13) becomes

$$V_S^{\mathrm{TE}} = -\int_0^{2\pi}\sin(\overline{\varphi} - \varphi)\cos(n\varphi) e^{jk_\rho b\cos(\overline{\varphi}-\varphi)} \cdot e^{j(k_x\Delta x + k_y\Delta y)} b\, d\varphi. \tag{A.14}$$

Integrating (A.14) and substituting the result into (A.8) yields

$$\tilde{H}_u = -I_V^{\mathrm{TE}}(k_\rho)(j)^{n-1}(2\pi n b)\sin(n\overline{\varphi}) \cdot \left[\frac{J_n(k_\rho b)}{k_\rho b}\right] e^{j(k_x\Delta x + k_y\Delta y)}. \tag{A.15}$$

The derivation for the TM component is very similar. Applying the SDI formulation yields

$$\tilde{H}_v = I_V^{\mathrm{TM}} V_s^{\mathrm{TM}} \tag{A.16}$$

where I_v^{TM} is defined as the TM component of the current in the equivalent transmission line model due to a series 1-V source at the center of the substrate and

$$V_S^{\mathrm{TM}} = -\left(-\tilde{M}_x\sin\overline{\varphi} + \tilde{M}_y\cos\overline{\varphi}\right). \tag{A.17}$$

Using (A.11) and (A.12), (A.17) can be written as

$$V_S^{\mathrm{TM}} = -\int_0^{2\pi}\cos(\overline{\varphi} - \varphi)\cos(n\varphi) e^{jk_\rho b\cos(\overline{\varphi}-\varphi)} \cdot e^{j(k_x\Delta x + k_y\Delta y)} b\, d\varphi. \tag{A.18}$$

Integrating (A.18) and substituting the result into (A.16) yields

$$\tilde{H}_v = -I_V^{\mathrm{TM}}(k_\rho)(j)^{n-1}(2\pi b)\cos(n\overline{\varphi}) J_n'(k_\rho b) e^{j(k_x\Delta x + k_y\Delta y)}. \tag{A.19}$$

Substituting (A.6) and (A.7) into (A.3) and using well-known trigonometric identities yields

$$R_{mn} = R_{mn}^{\mathrm{TE}} + R_{mn}^{\mathrm{TM}} \tag{A.20}$$

where

$$R_{mn}^{\mathrm{TE}} = -\frac{1}{(2\pi)^2}\int_0^{2\pi}\int_0^{\infty}\int_0^{2\pi} \tilde{H}_u \sin(\overline{\varphi}-\varphi^A)\cos(m\varphi^A) \cdot e^{-jk_\rho b\cos(\overline{\varphi}-\varphi^A)} bk_\rho\, d\overline{\varphi}\, dk_\rho\, d\varphi^A \tag{A.21}$$

and

$$R_{mn}^{\mathrm{TM}} = -\frac{1}{(2\pi)^2}\int_0^{2\pi}\int_0^{\infty}\int_0^{2\pi} \tilde{H}_v \cos(\overline{\varphi}-\varphi^A)\cos(m\varphi^A) \cdot e^{-jk_\rho b\cos(\overline{\varphi}-\varphi^A)} bk_\rho\, d\overline{\varphi}\, dk_\rho\, d\varphi^A. \tag{A.22}$$

The φ^A integrals in (A.21) and (A.22) can be evaluated in closed form; hence, substituting (A.15) into (A.21) and (A.19) into (A.22) yields

$$R_{mn}^{\mathrm{TE}} = (-j)^{m-1}j^{n-1}(mnb^2)\int_0^{2\pi}\int_0^{\infty} I_v^{\mathrm{TE}}(k_\rho) \cdot \sin(m\overline{\varphi})\sin(n\overline{\varphi})\left[\frac{J_m(k_\rho b)}{k_\rho b}\right] \cdot \left[\frac{J_n(k_\rho b)}{k_\rho b}\right] e^{j(k_x\Delta x + k_y\Delta y)} k_\rho\, dk_\rho\, d\overline{\varphi} \tag{A.23}$$

and

$$R_{mn}^{\mathrm{TM}} = (-j)^{m-1}j^{n-1}b^2\int_0^{2\pi}\int_0^{\infty} I_v^{\mathrm{TM}}(k_\rho)\cos(m\overline{\varphi})\cos(n\overline{\varphi}) \cdot J_m'(k_\rho b)J_n'(k_\rho b)e^{j(k_x\Delta x + k_y\Delta y)} k_\rho\, dk_\rho\, d\overline{\varphi}. \tag{A.24}$$

Finally, we normalize (A.23) and (A.24) using $k_\rho = k_o\beta$ and evaluate the $\overline{\varphi}$ integrals analytically, yielding the following results:

$$R_{mn}^{\mathrm{TE}} = \pi(-j)^{m-1}j^{n-1}mn(k_o b)^2\int_0^{\infty} \cdot I_v^{\mathrm{TE}}(\beta)\left[\frac{J_m(k_o\beta b)}{k_o\beta b}\right]\left[\frac{J_n(k_o\beta b)}{k_o\beta b}\right] \cdot \{j^{n-m}\cos[(n-m)\alpha]J_{n-m}(2\pi\beta\gamma) - j^{n+m} \cdot \cos[(n+m)\alpha]J_{n+m}(2\pi\beta\gamma)\}\beta\, d\beta \tag{A.25}$$

$$R_{mn}^{\mathrm{TM}} = \pi(-j)^{m-1}j^{n-1}(k_o b)^2\int_0^{\infty} \cdot I_v^{\mathrm{TM}}(\beta)J_m'(k_o\beta b)J_n'(k_o\beta b) \cdot \{j^{n-m}\cos[(n-m)\alpha]J_{n-m}(2\pi\beta\gamma) + j^{n+m} \cdot \cos[(n+m)\alpha]J_{n+m}(2\pi\beta\gamma)\}\beta\, d\beta \tag{A.26}$$

where

$$\alpha = \tan^{-1}\left(\frac{\Delta\overline{y}}{\Delta\overline{x}}\right) \tag{A.27}$$

$$\gamma = \Delta\overline{x}\cos\alpha + \Delta\overline{y}\sin\alpha \tag{A.28}$$

$\Delta\overline{x} = \Delta x/\lambda_o$, and $\Delta\overline{y} = \Delta y/\lambda_o$.

REFERENCES

[1] D. R. Jackson, J. T. Williams, A. K. Bhattacharyya, R. L. Smith, S. J. Buchheit, and S. A. Long, "Microstrip patch designs that do not excite surface waves," *IEEE Trans. Antennas Propagat.*, vol. 41, pp. 1026–1037, Aug. 1993.

[2] V. B. Davis, M. A. Khayat, S. Jiang, D. R. Jackson, J. T. Williams, and S. A. Long, "Characteristics of the shorted-annular ring reduced surface wave antenna," IEEE Trans. Antennas Propagat., to be published.

[3] J. R. Wait, *Electromagnetic Waves in Stratified Media*. New York: IEEE Press, 1996.

[4] ——, "Electromagnetic surface waves," *Adv. Radio Res.*, vol. 1, pp. 157–217, 1964.

[5] L. B. Felsen and N. Marcuvitz, *Radiation and Scattering of Waves*. New York: IEEE Press, 1994.

[6] V. B. Davis, J. T. Williams, D. R. Jackson, S. A. Long, and S. Jiang, "Effect of ground plane size on radiation patterns of reduced surface wave antennas," IEEE Trans. Antennas Propagat., to be published.

[7] R. F. Harrington, *Time-Harmonic Electromagnetic Fields*. New York: McGraw-Hill, 1961.

[8] W. F. Richards, Y. T. Lo, and D. Harrison, "An improved theory for microstrip antennas and applications," *IEEE Trans. Antennas Propagat.*, vol. AP-29, pp. 38–46, Jan. 1981.

[9] A. K. Bhattacharyya, "Characteristics of space and surface-waves in a multilayered structure," *IEEE Trans. Antennas Propagat.*, vol. 38, pp. 1231–1238, Aug. 1990.

[10] K. A. Michalski and D. Zheng, "Electromagnetic scattering and radiation by surfaces of arbitrary shape in layered media—Part I: Theory," *IEEE Trans. Antennas Propagat.*, vol. 38, pp. 335–344, Mar. 1990.

[11] M. D. Deshpande and M. C. Bailey, "Analysis of finite phased arrays of circular microstrip patches," *IEEE Trans. Antennas Propagat.*, vol. 37, pp. 1355–1360, Nov. 1989.

[12] N. Bleistein and R. A. Handelsman, *Asymptotic Expansion of Integrals*. New York: Dover, 1986.

[13] M. Abramowitz and I. E. Stegun, *Handbook of Mathematical Functions*: Nat. Bureau Stand. AMS 55, 1972.

[14] S. Barkeshli, P. H. Pathak, and M. Marin, "An asymptotic closed-form microstrip surface Green's function for the efficient moment method analysis of mutual coupling in microstrip antennas," *IEEE Trans. Antennas Propogat.*, vol. 38, pp. 1374–1383, Sept. 1990.

[15] T. Itoh, "Spectral domain immittance approach for dispersion characteristics of generalized printed Transmission lines," *IEEE Trans. Microwave Theory Tech.*, vol. MTT-28, pp. 733–736, July 1980.

[16] N. Marcuvitz, *Waveguide Handbook*. London, U.K.: Peter Peregrinus, ch. 1.

[17] T. Itoh, "A full-wave analysis method for open microstrip structures," *IEEE Trans. Antennas Propogat.*, vol. AP-29, pp. 63–68, Jan. 1981.

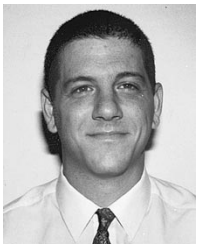

Michael A. Khayat (S'99) was born in Houston, TX, in 1972. He received the B.S.E.E. and M.S.E.E. degrees from the University of Houston, TX, in 1996 and 1999, respectively. He is currently working toward the Ph.D. degree in electrical engineering at the same university.

During the summer of 2000, he was with Compaq Computer Corporation, Houston, TX, researching wireless technologies for the Portable PC Division. His current interests include microstrip antenna design and computational electromagnetics.

Jeffery T. Williams (S'85–M'87–SM'97) was born in Kula, Maui, HW, on July 24, 1959. He received B.S., M.S., and Ph.D. degrees in electrical engineering from the University of Arizona, Tucson, in 1981, 1984, and 1987, respectively.

He joined the Department of Electrical and Computer Engineering, University of Houston, TX, in 1987, where he is now an Associate Professor. Prior to that, he was a Schlumberger-Doll Research Fellow at the University of Arizona. He spent four summers (1983–1986) at the Schlumberger-Doll Research Center, Ridgefield, CT, as a Research Scientist. From 1981 to 1982, he was a Design Engineer with Zonge Engineering and Research Organization, Tucson, AZ, and as a Summer Engineer at the Lawrence Livermore National Laboratory, Livermore, CA. He is a past Associate Editor for *Radio Science*. His research interests include the design and numerical analysis of high frequency antennas, antenna measurements, the application of high temperature superconductors in antenna systems, and leaky-wave propagation.

Dr. Williams is a past Associate Editor for the IEEE TRANSACTIONS ON ANTENNAS AND PROPAGATION. He is a member of URSI Commission B.

David R. Jackson (S'83–M'85–SM'95–F'99) was born in St. Louis, MO, on March 28, 1957. He received the B.S.E.E. and M.S.E.E. degrees from the University of Missouri, Columbia, in 1979 and 1981, respectively, and the Ph.D. degree in electrical engineering from the University of California, Los Angeles, in 1985.

From 1985 to 1991, he was an Assistant Professor in the Department of Electrical and Computer Engineering, University of Houston, TX. From 1991 to 1998, he was an Associate Professor in the same department, and since 1998, he has been a Professor there. He is currently an Associate Editor for the *International Journal of Radio Frequency and Microwave Computer-Aided Engineering*. He is a past Associate Editor for the *Journal Radio Science*. His current research interests include computer-aided design of microstrip antennas and circuits, microstrip antenna analysis and design, periodic structures, leaky-wave antennas, leakage effects in microwave integrated circuits, and bioelectromagnetics.

Dr. Jackson is a past Associate Editor for the IEEE TRANSACTIONS ON ANTENNAS AND PROPAGATION. He has also served as a past member of ADCOM for Antennas and Propagation Society (AP-S). He is presently serving as the Chapter Activities Coordinator for the AP-S Society of the IEEE and as the Chair of the Technical Activities Committee for URSI Commission B. He is also presently serving as a Distinguished Lecturer for the IEEE AP-S Society.

Stuart A. Long (F'91) was born in Philadelphia, PA, on March 6, 1945. He received the B.A. (*magna cum laude*) and M.E.E. degrees in electrical engineering from Rice University, Houston, TX, in 1967 and 1968, respectively, and the Ph.D. degree in applied physics from Harvard University, Cambridge, MA, in 1974.

He was employed as an Aerosystems Engineer in the antenna design group of General Dynamics, Ft. Worth, TX, from 1968 to 1969. From 1970 to 1974, he was a Teaching Fellow and Research Assistant in applied mathematics and applied physics at Harvard University. He was also a Research Assistant at Los Alamos Scientific Laboratories, Los Alamos, NM, for the summers of 1970 and 1971. In 1974, he joined the faculty at the University of Houston and served as Chairman of the Department of Electrical and Computer Engineering from 1984 to 1995 and again from 1998 to 1999 and as Associate Dean of the College of Engineering from 1995 to 1998. Presently, he is a Professor in the Department of Electrical and Computer Engineering. where he teaches a variety of undergraduate and graduate level classes in applied electromagnetics.

Dr. Long was elected to the Administrative Committee (AdCom) of the IEEE Antennas and Propagation Society (AP-S) for a three-year term in 1981 and again in 1989. He was organizer and General Chairman of the 1983 IEEE AP-S/URSI International Symposium and presently serves as the National Meetings Coordinator of AP-S. He was elected as Vice-President for 1995 and as President for 1996 of AP-S. He also served on the IEEE Technical Activities Board, was TAB Magazines Chair, and was a Member of the Periodicals Review Committee from 1997 to 1999. He is currently a Member-at-Large of the IEEE Publications Activities Board and is on the Spectrum Editorial Board. He received the Halliburton Award of Excellence as the Outstanding Teacher in Engineering at the University of Houston in 1983, the University Teaching Excellence Award in 1991, the Engineering Alumni Association's 1992 Distinguished Faculty Award, and the Outstanding Teacher in Electrical Engineering by the IEEE Eta Kappa Nu students in 1994. He also received the Senior Research Award from the College of Engineering in 1995. He is a member of Phi Beta Kappa, Tau Beta Pi, Sigma Xi, and Commission B of URSI. He was elected a member of the Electromagnetics Academy in 1990 and served as an IEEE Antennas and Propagation Society Distinguished Lecturer from 1992 to 1994. He is a registered Professional Engineer.